Unlocking Structure-Self-Assembly Relationships in Cationic Azobenzene Photosurfactants

Camille Blayo[a], Judith E. Houston[b], Stephen M. King[c] and Rachel C. Evans[d]

[a] School of Chemistry and CRANN, University of Dublin, Trinity College, College Green, Dublin 2, Ireland.

[b] Jülich Centre for Neutron Science (JCNS) at Heinz Maier-Leibnitz Zentrum (MLZ), Forschungszentrum Jülich GmbH, Lichtenbergstr. 1, 85748 Garching, Germany.

[c] ISIS Pulsed Neutron Source, STFC, Rutherford Appleton Laboratory, Didcot, Oxfordshire OX11 0QX, U.K.

[d] Department of Materials Science & Metallurgy, University of Cambridge, U.K.

Email: rce26@cam.ac.uk

ABSTRACT

Azobenzene photosurfactants are light-responsive amphiphiles that have garnered significant attention for diverse applications including delivery and sorting systems, phase transfer catalysis and foam drainage. The azobenzene chromophore changes both its polarity and conformation (*trans-cis* isomerization) in response to UV light, while the amphiphilic structure drives self-assembly. Detailed understanding of the inherent relationship between the molecular structure, physicochemical behaviour and micellar arrangement of azobenzene photosurfactants is critical to their usefulness. Here, we investigate the key structure-function-assembly relationships in the popular cationic alkylazobenzene trimethylammonium bromide (AzoTAB) family of photosurfactants. We show that subtle changes in the surfactant structure (alkyl tail, spacer length) can lead to large variations in the critical micelle concentration, particularly in response to light, as determined by surface tensiometry and dynamic light

scattering. Small-angle neutron scattering (SANS) studies also reveal the formation of more diverse micellar aggregate structures (ellipsoids, cylinders, spheres) than predicted based on simple packing parameters. The results suggest that while the azobenzene core resides in the effective hydrophobic segment in the *trans*-isomer, it forms part of the effective hydrophilic segment in the *cis*-isomer, due to the dramatic conformational and polarity changes induced by photoisomerization. The extent of this shift in the hydrophobic-hydrophilic balance is determined by the separation between the azobenzene core and the polar head group in the molecular structure. Our findings show that judicious design of the AzoTAB structure enables selective tailoring of the surfactant properties in response to light, such that they can be exploited and controlled in a reliable fashion.

KEY WORDS

Surfactant, azobenzene, light, self-assembly, micelle, small-angle neutron scattering, photoisomerization, critical micelle concentration

INTRODUCTION

Stimuli-responsive materials have attracted significant interest due to their potential applications as shape-memory systems,[1] molecular machines[2] or artificial muscles.[3] These materials change their physicochemical properties in response to one or more stimuli in their local environment, such as light,[4-5] pH[6] or heat.[7] Light is a very effective stimulus as it can be applied selectively at different wavelengths and intensities, with complete temporal and spatial control.[5, 8] The *trans*-*cis* photoisomerization of azobenzene in particular, has been extensively exploited in the design of light-responsive materials.[9-10] Upon irradiation with UV light, photoisomerization leads to dramatic changes in the size, shape and dipole moment of the molecule, which can be reversed through the application of blue light or heat.[11] In this context, azobenzene photosurfactants, in which the photoresponsive motif is located within a surfactant structure (usually the tail), are particularly attractive due to the combination of surface activity, self-assembly and photoresponse in a single molecule.[12] These unique properties have led to the investigation of azobenzene photosurfactants in a variety of applications, which have been recently reviewed,[13] and include microfluidic devices,[8] cargo delivery[14] and micellar catalysis.[15]

Like conventional surfactants, when present above a critical concentration in aqueous solution, photosurfactants tend to self-assembly into micelles.[12] For ionic surfactants in water, the absolute value of the critical micelle concentration (CMC) is largely determined by the length of the hydrophobic segment, which provides the driving force for self-assembly, with long hydrophobic segments leading to low CMCs.[16] The shape, size and long-range organisation of the self-assembled aggregates are influenced by concentration, temperature and ionic strength of the medium, while the molecular packing within micelles is largely dependent on the shape and volume of individual molecules.[17] In photosurfactants, the azobenzene group is usually incorporated within the hydrophobic segment of the *trans*-

isomer.[13] However, photoisomerization to the *cis*-isomer induces a significant change in the effective length and volume of the surfactant tail,[18] and also leads to a large increase in the dipole moment (μ = 3.0 D for the *cis*-azobenzene core[19]), which makes the molecule significantly more hydrophilic. As such, it can be difficult to distinguish the effective hydrophilic and hydrophobic segments of the molecule, particularly if there is only a small separation between the azobenzene core and the head group.[20-21] A further complication arises from the fact that photoisomerization never results in complete conversion and instead a photostationary state comprised of an excess of the predominant isomer is obtained.[22]

Given these challenges, it is perhaps not surprising that there have been limited structure-self-assembly studies on azobenzene photosurfactants.[23-24] The most studied structure is a cationic azobenzene photosurfactant bearing a trimethylammonium bromide (TAB) polar head group, which is separated from the azobenzene (Azo) core by an alkoxy spacer (O-R_2). A pendant alkyl tail (R_1) completes the hydrophobic segment of the surfactant (AzoTAB, Figure 1). AzoTAB surfactants have received significant attention for their potential applications, for example in the design of light-responsive gels[25-27] and DNA,[28-30] modified graphene oxide,[31-32] photomanipulation of droplets,[8] templating[33] and photoluminescent complexes.[34] In contrast, little has been done to determine the relationship between molecular design and function in AzoTABs. Hayashita *et al*. studied the effect of the length of the hydrophobic segment ($R_1 + R_2 < 10$) of AzoTABs in the *trans*- and *cis*- forms and determined that an increase in the length of the alkyl tail (R_1) led to a decrease in both the absolute conductivity and CMC.[35] Other studies have investigated the interaction of C_4AzoOR_2TAB, with different spacer lengths (R_2 = 6, 8, 10, 12) with oppositely-charged particles (microgels[25], DNA[29]). Elongated spacers were shown to result in more hydrophobic AzoTABs, which facilitated compaction of DNA, while photoisomerization led to the reverse decompaction.[36] Similarly, Diguet *et al.* reported that for C_4OAzoOR_2TAB (R_2 = 2, 5, 8)

optimal control of DNA compaction required a compromise in the photosurfactant design, between the best reversibility (short spacer length) and compaction efficiency (long spacer length).[30] Only a few studies have investigated the size and shape of AzoTAB micelles above the CMC in detail, with the primary focus centred on the effect of photoisomerization on the general aggregate structure.[32, 37-38]

In this study we systematically investigate structure-function-self-assembly relationships in the AzoTAB family at short-to-intermediate chain lengths (up to 14 carbons, excluding the azobenzene core). To achieve this, we have rationally designed a series of structures that enable us to explore and extend the current limits of available AzoTABs in the literature. Our primary focus is to elucidate how the length of the hydrophobic segment, and the relative sizes of the spacer and alkyl tails of which it is composed, influence the surface tension, CMC and micelle shape and size. Small-angle neutron scattering studies are used to examine the effect of concentration, temperature and photoisomerization on the micellar structure. In particular, we investigate how the relative separation between the azobenzene core and the head group (controlled by spacer length) affects the effective head-to-tail volume upon photoisomerization. The application of packing parameters[39] to predict the aggregate shape for non-conventional surfactants such as AzoTABs will also be examined. Our end goal is to provide key insight into the structural factors controlling surface activity and self-assembly in AzoTAB surfactants, which will enable the strategic design of new structures whose properties are specifically tailed towards their intended application as stimuli-responsive materials.

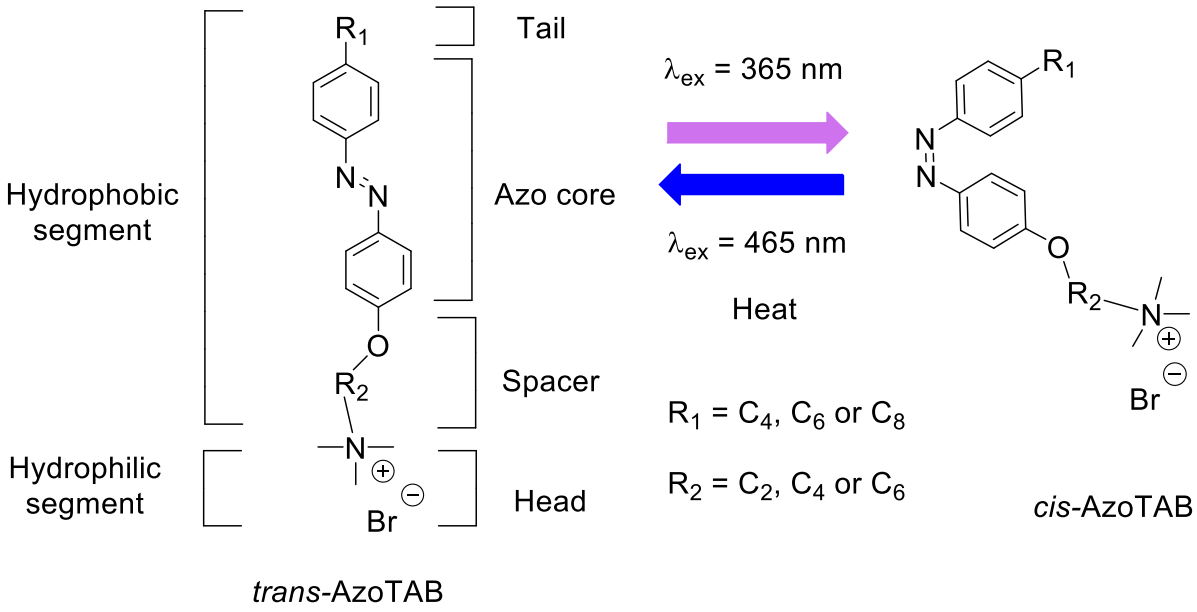

Figure 1. Molecular structure of the AzoTAB photosurfactants investigated in this study. R_1 corresponds to the pendant alkyl tail and R_2 indicates the spacer. The *trans-cis* photoisomerization occurs at λ_{ex} = 365 nm and the reversible *cis-trans* photoisomerization at λ_{ex} = 465 nm or with heat.

EXPERIMENTAL

Materials. AzoTAB photosurfactants were synthesized following a slight modification to a previously reported method.[40] Full details of the synthetic procedures and associated characterisation can be found in the Supporting Information (SI, Figure S1-15). To the best of our knowledge, **C_6AzoOC_4TAB** and **C_8AzoOC_6TAB** are new compounds, while **C_4AzoOC_4TAB**,[32, 35] **C_8AzoOC_2TAB**[35] and **C_4AzoOC_6TAB**[41] have been synthesized previously.

Photoirradiation Studies. *Trans-cis* photoisomerization was performed by exposing aqueous solutions (3 mL) of the photosurfactant in a quartz cuvette (10 mm path length) on one side to a UV light-emitting diode (LED) (Prolight®) with an illumination wavelength of 365 nm and an incident power output of 5 mW cm^{-2} in a custom-built dark box. For all experiments performed in this study, the progress of photoisomerization was followed by UV/Vis absorption spectroscopy. The photostationary state was determined to be reached when the

absorbance at 315 nm (*cis*-isomer) or 350 nm (*trans*-isomer) did not increase further upon continued irradiation (Figure S16, SI). The photostationary state was typically obtained after 3 min irradiation for dilute solutions (<20 mM) and was comprised of ~95% *cis*- and ~5% *trans*-isomers.

Surface Tensiometry (ST). Surface tensiometry measurements were performed on a Kibron EZ-Pi^{plus} surface tensiometer using a DyneCups plastic cuvette (3 mL) and a DyneProbe ring. The instrument uses the Du Noüy ring method to record ST data. The method enables the interfacial force between two media to be recorded. The obtained data were recorded on AquaPiPlus software and were averaged from 5 runs for each sample. Millipore water was used as a reference sample.

Dynamic Light Scattering (DLS). DLS measurements were performed using a Zetasizer Nano series nano-ZS instrument (Malvern Instruments, U.K.). The apparatus is equipped with a He-Ne laser (λ_{ex} = 633 nm, 4.0 mW power source). Detection of the scattering intensity was done at a backscattering angle of 173°. Millipore water was filtered 5 times, prior to preparation of the solutions. For each sample, three measurements were performed, each taking an average of 15 scans. Cumulant analysis of the autocorrelation function was used to determinate the polydispersity and the mean hydrodynamic diameter (*Z*-average) of each sample.

Small-Angle Neutron Scattering (SANS). SANS measurements were performed on the LOQ beamline at the ISIS Pulsed Neutron Source (STFC Rutherford Appleton Laboratory, Didcot, U.K.).[42] A simultaneous q-range of 0.009-0.24 Å^{-1} was achieved using an incident wavelength range of 2.2-10.0 Å separated by time-of-flight over a sample-detector distance of 4.1 m, where $q = 4\pi\sin(\theta/2)/\lambda$, λ is the incident wavelength and θ is the scattering angle. Samples were prepared in D_2O to ensure good neutron scattering contrast and placed in quartz

cuvettes (Hellma UK, Type 120, 1 mm pathlength). Each raw scattering data set was corrected for the detector efficiency, sample transmission and background scattering and converted to scattering cross-section data ($\partial\Sigma/\partial\Omega$ *vs.* q) using the software Mantid.[43] These data were converted to absolute scattering intensity (cm^{-1}) by comparison with the scattering from a standard sample (a solid blend of hydrogenated and perdeuterated polystyrene) in accordance with established procedures.[44] SANS profiles were then fitted using to Sphere,[45] oblate Ellipsoid[46] or Elliptical Cylinder models[46] including polydispersity as described in the text using nonlinear least-squares optimization with the SasView program (version 4.0.1).[47] Full details of the models can be found in the SI. Validation of the model fits was achieved using the theoretical mass of dry material (φ_{dry}) that the fit returned (see section 5.2.1 of the S.I. for full details).

Cryogenic Scanning Emission Microscopy (Cryo-SEM). Cryo-SEM measurements were performed using a Zeiss-Ultra Scanning Electron Microscope at an accelerating voltage of 2-5 kV using an In-lens detector. Samples were plunged into sub-cooled liquid N_2 to freeze and then transferred *in-vacuo* to the cold stage of the SEM cryo-preparation chamber.

RESULTS

Design of AzoTABs

AzoTAB structures were designed to explore a range of intermediate lengths (C8, C10, C14) for the hydrophobic segment, which comprises the Azo core, a moderate length alkyl tail (R_1 = 4, 6 or 8) and a short to moderate length spacer (R_2 = 2, 4 or 6). The relative lengths of the spacer and the alkyl chain control the extent at which the Azo group is embedded in the hydrophobic segment. These AzoTABs were chosen to explore molecular dimensions that supplement previously reported structures.[48-49] Detailed sample compositions are shown in Table 1. The samples are denoted as **C_xAzoOC$_y$TAB**, where x corresponds to the number of

carbon atoms in the alkyl tail and *y* corresponds to the number of carbon atoms in the spacer. **C_8AzoOC_2TAB** and **C_4AzoOC_6TAB** have been reported previously, but a detailed investigation of the surface activity and micellar structure was not performed.[29, 35] **C_4AzoOC_4TAB** is the most extensively studied AzoTAB structure[32, 35] and is included as a benchmark for the other compounds.

The self-assembly of conventional surfactants above the CMC can be reasonably approximated from the packing parameter, P, which is given by $P = V/al$, where V is the volume of the hydrophobic tail of the surfactant, l is the tail length and a is the effective head group area.[39] The packing parameter predicts the shape and size of micellar aggregates based on geometrical considerations.[50] Calculations of V and l for conventional surfactants are usually given by the Tanford equations[51] and, for a given a, the V/l ratio remains constant, independent of the hydrophobic tail length.[17] The calculated packing parameters for the *trans*- and *cis*-isomers of the AzoTABs are shown in Table 1 (see Table S4 in the SI for calculation of P). Similar to the analogous cationic alkyltrimethylammonium bromide surfactants with no Azo core,[52] spherical micelles are expected for all investigated AzoTABs, in both isomeric forms. However, while the packing parameters for the *trans*- and *cis*-isomers appear to be independent of the molecular structure, these estimates do not consider the effect of the position of the azobenzene core within the photosurfactant. In particular, short spacers and long alkyl chains are expected to significantly affect the hydrophobicity of AzoTABs, leading to stark changes in the physicochemical properties upon photoisomerization of the azobenzene core.[35]

Table 1. Molecular structure and calculated packing parameters, P, of the AzoTABs studied. R_1 + R_2 corresponds to the total length of the hydrophobic segment (excluding the Azo core), varying from short (R_1 + R_2 = 8) to intermediate (R_1 + R_2 = 14). From the calculated P values, all AzoTABs (in both isomeric forms) are expected to form spherical micelles ($0.286 < P < 0.335$).[53]

AzoTAB	R_1 (Tail)	R_2	R_1+ R_2	P_{trans}	P_{cis}

		(Spacer)			
C_4AzoOC_4TAB	4	4	8	0.29	0.34
C_4AzoOC_6TAB	4	6	10	0.29	0.34
C_6AzoOC_4TAB	6	4	10	0.29	0.34
C_8AzoOC_2TAB	8	2	10	0.29	0.34
C_8AzoOC_6TAB	8	6	14	0.30	0.34

Surface Tension, Solubility and the CMC.

The CMCs of AzoTABs in water (20 °C) were determined for both isomers using surface tensiometry and dynamic light scattering. As a representative example, Figure 2a shows the variation in surface tension as a function of concentration for **C_4AzoOC_6TAB**. The CMC is reached when the surface tension becomes independent of surfactant concentration,[54] at 0.40 mM and 1.05 mM for the *trans*- and *cis*-forms, respectively. The CMC was confirmed by DLS, whereby the intensity of scattering light increases significantly upon the onset of micelle formation (Figure 2b). The CMCs determined for all AzoTABs by both ST and DLS are summarized in Table 2. It is worth noting that the Krafft temperature of alkyltrimethylammonium bromide surfactants (*e.g.* C_{16}TAB) is known to be around 25 °C in water.[55] Interestingly, among the AzoTABs studied here, only **C_6AzoOC_4TAB** displays low solubility in water at 20 °C, and flocculates, suggesting that this temperature is below the Krafft point.[56] Controlled heating of **C_6AzoOC_4TAB** (5 mM in water) confirmed the Krafft temperature to be 27 °C. The values for the CMC obtained are in good agreement with those previously reported for AzoTAB surfactants.[29, 32, 35] The absolute values of the surface tension isotherm above the CMC are in good agreement with reported values for azobenzene photosurfactants,[32] with the longest hydrophobic segment showing the lowest surface tension (*i.e.* $R_1 + R_2 = 14$).

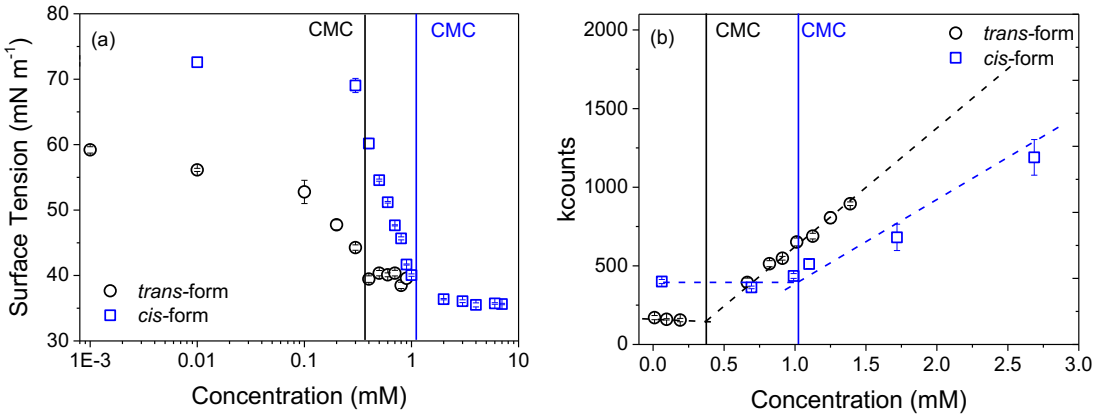

Figure 2. Determination of the CMC of **C_4AzoOC$_6$TAB** in water at 20 °C. Variation of (a) surface tension and (b) light scattering as a function of concentration. The data points show the trend before (*trans*-form, black circles) and after irradiation with UV light at λ_{ex} = 365 nm for 5 min (predominantly *cis*-form, blue squares). The CMC values are obtained from the intersection between the two trends (solid lines). The error bars show the standard deviation of the mean values obtained over 5 (ST) or 3 (DLS) measurements. The dashed lines serve only to guide the eye.

Table 2. Summary of the CMCs obtained for AzoTABs by surface tensiometry (ST) and dynamic light scattering (DLS) at 20 °C.

AzoTAB	*trans*-CMC (mM)		*cis*-CMC (mM)		*trans*-/*cis*-CMC (mM)
	ST	DLS	ST	DLS	Literature
C_4AzoOC$_4$TAB	1.10 ± 0.02	1.2 ± 0.1	2.50 ± 0.02	2.7 ± 0.2	1.2/2.7[b] ; 1.0/2.0[c]
C_4AzoOC$_6$TAB	0.40 ± 0.02	0.4 ± 0.1	1.05 ± 0.02	1.1 ± 0.1	~0.5/NR[d]
C_6AzoOC$_4$TAB[a]	0.19 ± 0.03	0.2 ± 0.1	0.62 ± 0.03	0.7 ± 0.1	
C_8AzoOC$_2$TAB	0.34 ± 0.02	0.3± 0.1	0.82 ± 0.03	0.8 ± 0.1	0.3/0.8[b]
C_8AzoOC$_6$TAB	0.09 ± 0.02	0.1 ± 0.1	0.15 ± 0.03	0.2 ± 0.1	

[a] Corresponds to the critical aggregation concentration at 25 °C. [b] From Hayashita *et al.*[35] – determined by conductivity (T = 25 °C). [c] From McCoy *et al.*[32] – determined by pendant drop tensiometry (T = not specified). [d] From Zakrevskyy *et al.*[29] – determined by isothermal titration calorimetry (T = 25 °C), *cis*-isomer not reported (NR).

Three key trends can be identified upon comparison of the CMCs of the AzoTABs studied here with those previously reported as a function of the alkyl tail length (R_1) and the spacer length (R_2) for both the *trans*- and *cis*-isomers. For a given surfactant, the CMC of the *cis*-isomer is always higher than that of the *trans*-isomer, which can be rationalized based on the increased dipole moment, and thus hydrophilicity, upon photoisomerization. Secondly, the hydrophobic driving force for micellization is driven by the total length of the hydrophobic

segment of the structure, with a larger length (*i.e.* $R_1 + R_2$) leading to a lower CMC. This has been previously demonstrated for short hydrophobic segments ($R_1 + R_2 \leq 8$)[35] and is confirmed here for much longer hydrophobic segments (up to $R_1 + R_2 = 14$), enabling the CMCs to be tuned from mM to μM. Finally, for a fixed hydrophobic segment length, a longer alkyl tail (and thus a shorter spacer) leads to a smaller CMC, for example **C_4AzoOC$_6$TAB** > **C_8AzoOC$_6$TAB** (Table 2 and Figure S17-20, SI). Similarly, for a fixed alkyl chain length, the CMC decreases as the spacer length increases.

The difference in CMC (ΔCMC) for the *cis*- and *trans*-isomers as a function of the total number of carbons in the hydrophobic segment ($R_1 + R_2$) is shown in Figure 3. The ΔCMC is an important parameter as it represents the range of concentrations in which micelles exist in the *trans*-form only but are expected to return to unimers upon photoisomerization to the *cis*-isomer. This property has previously been exploited for the reversible encapsulation and release of small molecules, for example for catalysis[57] or drug release.[58] There is an apparent sweet spot for obtaining the maximum ΔCMC, which occurs for a total hydrophobic segment length of six carbons, irrespective of the tail and spacer lengths from which the segment is composed. As the total hydrophobic segment length is increased or decreased, the magnitude of the ΔCMC decreases significantly. If we consider the extreme cases, *i.e.* a very short or very long hydrophobic segment, the low ΔCMC can be rationalized. For short hydrophobic segments, the Azo core dominates both the length and the volume, and the difference between the hydrophobic driving force for micellization (dominated by the alkyl tail) for the two isomers is small. Similarly, for long hydrophobic segments, the longer alkyl tail and/or spacer increases the flexibility of the hydrophobic segment in both isomers, leading to an increase in the free volume irrespective of photoisomerization. For a hydrophobic segment length of $R_1 + R_2 = 6$, there is an apparent compromise between these two factors, whereby the free volume of the hydrophobic segment,

and therefore packing of the molecules in the micelle, is controlled predominantly by the photoisomerization of the Azo core.

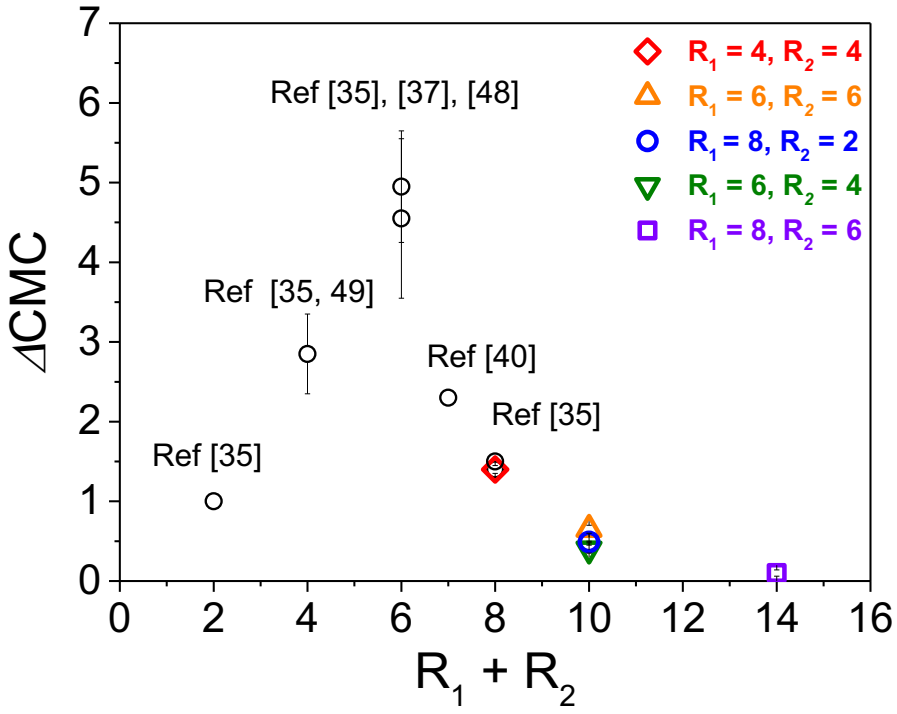

Figure 3. Comparison of the difference in CMC (ΔCMC) for *cis*- and *trans*-isomers of AzoTABs as a function of the total number of carbons in the hydrophobic segment ($R_1 + R_2$). Data are presented from this study (coloured circles) and previous reports (black circles). The errors bars result from different reported CMC in the literature.

Analysis of the absolute values reveals that an apparently larger ΔCMC is obtained for a longer spacer length, *i.e.* **C_2AzoOC_4TAB** > **C_4AzoOC_2TAB**. If we consider the homologous series of ($R_1 + R_2 = 10$) AzoTABs, the same trend is observed, with the absolute value of ΔCMC increasing with the spacer length, *i.e.* **C_4AzoOC_6TAB** > **C_8AzoOC_2TAB**. This suggests that the spacer length contributes a more important role to the effect that photoisomerization has on the packing of the molecules within the micelles. The spacer separates the hydrophilic head group from the Azo core, which is nominally hydrophobic in the *trans*-form. However, the increase in the dipole moment upon photoisomerization renders the Azo core more hydrophilic. As such, for short spacer lengths, the separation between the

polar head group and the Azo core is small, which could indicate that photoisomerization leads to an increase in the effective head group area of the molecule to include the now polar Azo core.

Above the CMC: Size and Shape of AzoTAB Micelles

Effect of concentration. SANS experiments were carried out to investigate the size and shape of AzoTAB micelles formed above the CMC as a function of the molecular structure. Figure 4 presents the SANS profiles for the AzoTABs in D_2O as a function of concentration (T = 20 °C). The SANS window for these experiments is calculated to be 10 to 1000 Å ($d = 2\pi/q$), which is suitable for the observation of micellar aggregates (~30 Å).[59] Scaling concepts were initially used to assess the data in the intermediate q-regime (q = 0.03-0.01 Å^{-1}). For **C_4AzoOC$_4$TAB**, **C_4AzoOC$_6$TAB** and **C_8AzoOC$_2$TAB** at 5 mM (Figure 4a-c, red squares), the SANS data scale as ~q^{-4} and level off as a Guinier plateau at low-q (q < 0.02 Å^{-1}), which is consistent with the formation of spherical-like aggregates.[60] Fitting of these SANS data to an oblate Ellipsoid model[46] yielded a short equatorial radius (R) of 25, 25 and 20 Å and a long equatorial radius (L) of 39, 45 and 52 Å for **C_4AzoOC$_4$TAB**, **C_4AzoOC$_6$TAB** and **C_8AzoOC$_2$TAB**, respectively (Table 3). The representative structure of an oblate ellipsoid is shown in Figure 4f. These values are in excellent agreement with values reported for both conventional cationic alkylammonium bromide surfactant solutions such as C_{16}TAB above the CMC (R~20 Å, L~30 Å),[61] previously reported AzoTAB structures (see Table 3), and the estimated lengths of the hydrophobic segment (Table S4). The fits were validated using Guinier analysis[62] to determine the radius of gyration (R_g), which yielded comparable values (see Table S2 and Figure S21, SI). It appears from the fitted parameters that the short radius, R, is not affected by the length of the hydrophobic segment or by the position of the azobenzene core within it, and remains around 20-25 Å. In contrast, the long equatorial

radius, *L*, increases with the length of the hydrophobic segment, which suggests that micellar growth occurs mainly in this direction.

The SANS data of **C_8AzoOC_6TAB** in D_2O at 5 mM (Figure 4d) decay as $\sim q^{-3.2}$ over a large *q* window (0.05-0.1 $Å^{-1}$) and tend towards a Guinier plateau at low-*q*, which suggests the formation of more elongated micelles. Fitting of the data to the oblate Ellipsoid Model[46] leads to radii of *R* = 28 Å and *L* = 88 Å. Despite the significant differences in the visual appearance of the SANS profiles, the *R* and *L* radii follow the trend in the dimensions of **C_4AzoOC_4TAB**, **C_4AzoOC_6TAB** and **C_8AzoOC_2TAB** described above and confirm that micelles grow preferentially in the *L* direction. Additionally, the eccentricity of the aggregates formed, defined as $\varepsilon = (1-R^2/L^2)^{0.5}$ suggests the formation of very flat ellipsoids ($\varepsilon = 0.95$). Finally, the SANS profile of **C_6AzoOC_4TAB** in D_2O at 5 mM decays as $\sim q^{-0.8}$ in the intermediate *q*-region (Fig 4e), which suggests the formation of more cylindrical structures. Fitting of the scattering profile to the Elliptical Cylinder model[46] leads to radii *R* of 28 Å and *L* of 49 Å, with a height of $H \approx 364$ Å. Although, this SANS profile differs from the other AzoTABs discussed above, it has been shown that cylindrical structures are spontaneously obtained for cationic CTAB surfactants with *ca*. 16 carbons in the hydrophobic tail in salt-free conditions.[63] **C_6AzoOC_4TAB** exhibits comparable *R* and *L* radii as the other AzoTABs with a hydrophobic segment length of C10 (*i.e.* **C_4AzoOC_6TAB** and **C_8AzoOC_2TAB**). For all AzoTABs studied, the aggregation number, N_{agg}, determined from the ratio of the volume of dry aggregates to the hydrophobic volume of one unimer (see SI) was found to increase with the total length of the hydrophobic segment (Table 3). Specifically, aggregates with a longer alkyl tail (R_1) contain more unimers per micelle than AzoTABs with a small R_1. This follows the conclusions drawn above for the trend in the CMC, where R_1 drives the formation of micelles for the *trans*-isomers of AzoTABs.

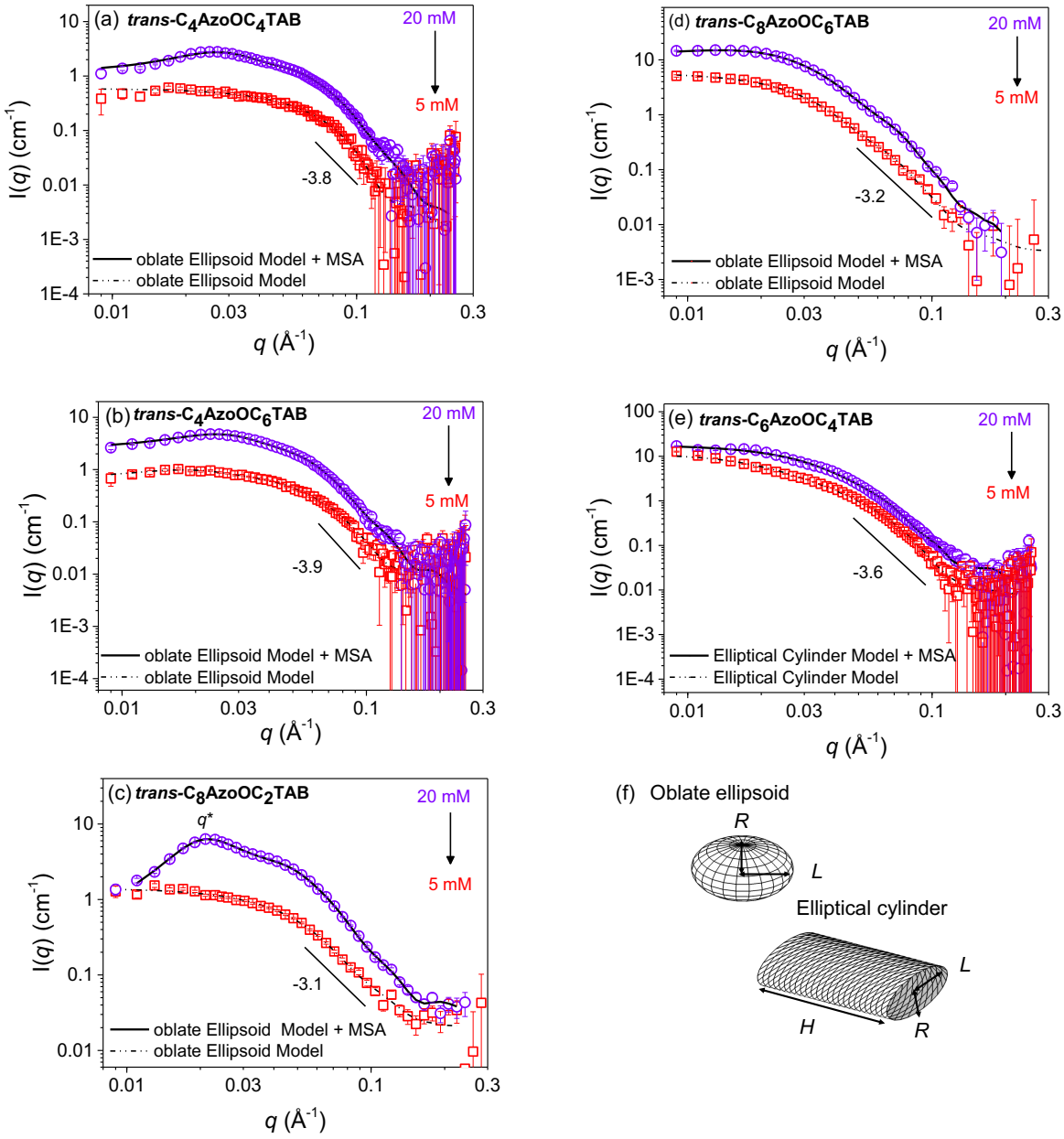

Figure 4. Effect of concentration on the SANS profiles of the *trans*-isomers of AzoTABs in D_2O at 20 °C. (a) **C_4AzoOC4$_4$TAB**, (b) **C_4AzoOC$_6$TAB**, (c) **C_8AzoOC$_2$TAB**, (d) **C_8AzoOC$_6$TAB** and (e) **C_6AzoC$_4$TAB** in D_2O at 20 mM (purple circles) and 5 mM (red squares). The black lines correspond to fits of the oblate Ellipsoid model or the Elliptical cylinder model as described in the text. At 20 mM, the Hayter-Penfold (MSA) structure factor is included in the fits. (f) Representative structures of oblate ellipsoids and elliptical cylinders, with *R* and *L* being the polar and equatorial radii, respectively, and *H* the length of the cylinder.

The SANS profiles show significant changes upon increasing the concentration to 20 mM. At low-*q* a Guinier plateau remains for **C_4AzoOC$_4$TAB**, **C_4AzoOC$_6$TAB** and **C_8AzoOC$_2$TAB**, but a shoulder appears at $q^* \approx 0.03$ Å^{-1}, which is attributed to repulsive interactions between the positively-charged micelles. To account for this, a Hayter-Penfold

(MSA) structure factor[64] was coupled with the appropriate form factor to model these profiles (see SI for further details). The obtained radii upon fitting to the oblate Ellipsoid model confirm that with increasing AzoTAB concentration, micellar growth proceeds along the *L* axis. Moreover, for a fixed alkyl tail length, this effect becomes more pronounced with an increase in the spacer length, such that for **C_4AzoOC$_2$TAB**[37], **C_4AzoOC$_4$TAB** and **C_4AzoOC$_6$TAB,** *L* values of 39 Å, 41 Å and 50 Å are obtained, respectively.

For a fixed hydrophobic segment length (R_1 + R_2 = 10), further differences in the micellar growth are observed. While **C_8AzoOC$_2$TAB** (Figure 4c) forms the most elongated micelles at 5 mM, further micellar growth is not observed upon increasing the concentration to 20 mM, and the micelles appear to become less stretched (decrease in ε from 0.92 to 0.89). This is accompanied by an increase in the scattering intensity at q^*, indicating an increase in the number of interparticle interactions and thus that the formation of new micelles is favoured over growth. In contrast, **C_4AzoOC$_6$TAB** micelles (Figure 4b) grow preferentially along the *L* axis with increasing concentration and by 20 mM reach the same size as **C_8AzoOC$_2$TAB**. At 5 mM, **C_6AzoOC$_4$TAB** forms cylindrical micelles, however with increasing concentration, the micellar parameters obtained from a fit to this model change significantly, suggesting growth along the *L* axis, which is accompanied by a significant decrease in the height of the cylinder from H = 363 Å to H = 162 Å. This suggests that a transition from a cylindrical to ellipsoidal structure may occur at higher concentrations, which is supported by a good fit of the data to the oblate Ellipsoid model (see Figure S23, SI). Finally, **C_8AzoOC$_6$TAB** shows similar behaviour to **C_8AzoOC$_2$TAB**, with no significant micellar growth or change in the micelle shape observed upon increasing the concentration. This suggests that the length of the alkyl tail determines both the size and the growth of the micelles formed.

Table 3. Summary of the parameters obtained for model fitting to the SANS profiles of *trans*-AzoTABs. For the structures investigated here, the fitted parameters are obtained as described in the text. All samples are in D_2O at 20 °C. Representative data from the literature are also included for comparison. ε refers to the eccentricity of the ellipsoidal structure only. q^* refer to the interference maximum where interparticle interactions become more significant and N_{agg} is the aggregation number for the micelle. A polydispersity of 0.1 was applied to all polar and equatorial radii to account for a polydisperse micellar population.

***trans*-AzoTAB**	**Conc. (mM)**	**Form factor $P(q)$**	***R*** **(Å)**	***L*** **(Å)**	***H*** **(Å)**	***ε***	***q**** **(Å^{-1})**	N_{agg}
C_4AzoOC_2TAB[a]	10	Ellipsoid	≈21	≈39	-	-	-	-
C_4AzoOC_4TAB[b]	5	Ellipsoid	≈18	≈40	-	-	-	-
C_4AzoOC_4TAB	5	Oblate	25 ± 3	39 ± 2	-	0.77	-	90 ± 14
	20	Ellipsoid[c]	24 ± 1	41 ± 1	-	0.81	0.025	165 ± 10
C_4AzoOC_6TAB	5	Oblate	25 ± 1	45 ± 1	-	0.83	-	119 ± 13
	20	Ellipsoid[c]	26 ± 1	50 ± 1	-	0.85	0.024	255 ± 24
C_8AzoOC_2TAB	5	Oblate	20 ± 1	52 ± 1	-	0.92	-	209 ± 21
	20	Ellipsoid[c]	24 ± 1	53 ± 1	-	0.89	0.021	309 ± 22
C_8AzoOC_6TAB	5	Oblate	28 ± 1	88 ± 1	-	0.95	-	669 ± 30
	20	Ellipsoid[c]	29 ± 1	87 ± 1	-	0.94	0.022	753 ± 27
C_6AzoOC_4TAB	5	Elliptical	28 ± 1	49 ± 1	364 ± 11	0.82	-	-
	20	Cylinder[c]	27 ± 1	53 ± 1	162 ± 2	0.86	0.019	-

[a] From Akamatsu *et al.*[37] [b] From McCoy *et al.*[32] [c] Hayter-Penfold structure factor for electrostatic interactions included in this fit as described in the text.

For all AzoTABs, the micellar structures become significantly drier upon increasing the surfactant concentration, irrespective of the shape, which appears to reach a limit 20-25%, and has been assumed to be concentrated around the polar head region (Table S2).[65-66] The decrease in the water content is consistent with increased packing between molecules as indicated by the increase in the aggregation number. **C_6AzoO_4TAB** is the only exception, forming significantly more wet aggregates at 5 mM (X_{Solv} = 62%), which decreases to X_{Solv} = 36% at 20 mM, which is consistent with the different aggregate shape formed for this AzoTAB.

Effect of Photoisomerization. Figures 5a and 5b show the SANS profiles of **C_4AzoOC_4TAB** and **C_4AzoOC_6TAB** in D_2O (20 mM) before and after irradiation at 365 nm. The scattering profiles of the *cis*-isomers are shifted towards high q, with q^* from q = 0.025 to 0.035 Å^{-1} and

q = 0.023 to 0.039 Å^{-1}, for **C$_4$AzoOC$_4$TAB** and **C$_4$AzoOC$_6$TAB** respectively, which indicate that micelles are more closely packed following photoisomerization. A Guinier plateau remains visible at low q followed by an abrupt decay which scales as ~$q^{-4.5}$. For **C$_4$AzoOC$_4$TAB**, fitting of the SANS data to the Sphere model[45] gave smaller, wet micelles (58% solvent) with a radius R of 26 Å and a low aggregation number (N_{agg} = 42). Increasing the spacer length by 2 carbons, whilst keeping the same alkyl chain R_1 (**C$_4$AzoOC$_6$TAB**), leads to dryer (35%) and slightly larger micelles (R = 26 Å, N_{agg} = 67). The SANS profile of *cis*-**C$_8$AzoOC$_2$TAB** can also be fitted with the Sphere model, leading to small (R = 25 Å) and dry (17%) aggregates. The Hayter-Penfold structure factor is required to produce good fits to the data, due to the large q^* at 0.038 Å^{-1}, which leads to a decrease in the estimated interparticle distance from 299 Å to 165 Å (Figure 5c). The shift in q* upon photoisomerization is the highest of all the AzoTABs studied here, suggesting a very closely packed environment. For the same hydrophobic segment length, the calculated radii follow the order **C$_4$AzoOC$_6$TAB > C$_4$AzoOC$_4$TAB** > **C$_8$AzoOC$_2$TAB,** where this time the spacer length seems to control the size of the micelle.

Figure 5d shows the SANS data and fits for *trans*- and *cis*-**C$_8$AzoOC$_6$TAB** in D_2O, in which a large difference in the scattering profiles of the two isomers is observed. After photoisomerization, a slight upturn is observed at q = 0.03 Å^{-1} followed by a sharp decay of ~$q^{-3.9}$. While the scattering data for both isomers are best described by the oblate Ellipsoid model[46] coupled with the Hayter-Penfold structure factor, there are stark differences between the obtained fitting parameters. The oblate ellipsoidal micelles formed by the *cis*-isomer are much smaller (R = 23 Å, L = 36 Å) and less flat than the *trans* counterparts (R = 29 Å, L = 87 Å), with an eccentricity of 0.77, indicating that the packing of unimers along the L axis is less favourable in the *cis*-micelles. Finally, the SANS profile of *cis*-**C$_6$AzoOC$_4$TAB** is very similar to that of the *trans*-form and could also be fit to the Elliptical Cylinder model,[46] to

give R = 22 Å, L = 46 Å and H = 260 Å, which are in good agreement with the fitting parameters for the *trans*-isomer (Figure 5e). As the presence of the *cis*-isomer was confirmed optically by UV/Vis absorption spectroscopy, before and after the SANS measurements (Figure S24), it appears that the bent *cis*-form can be accommodated quite effectively within the elliptical cylinder structure, with minimal changes to the structural parameters. It is worth noting here that complete conversion to the *cis*-isomer is never achieved, with a small fraction of *trans*-isomer (~5%) remaining in solution due to the photostationary state (Figure S15).

For all samples, the fitting parameters were validated by model-independent analysis of the radius of gyration (Figure S21, Table S3). The SANS data for the *cis*-isomers of all the AzoTABs in D_2O (5 mM) were also collected and fitted to the same models used for the corresponding sample at 20 mM (see Table 4 for obtained fitting parameters). As expected, at the lower concentration, the obtained micelles were smaller and wetter with a lower N_{agg}.

Table 4. Summary of the parameters obtained for model fitting to the SANS profiles for *cis*-AzoTABs. For the structures investigated here, the fitted parameters are obtained as described in the text. All samples are in D_2O at 20 °C. Representative data from the literature are also included for comparison. ε refers to the eccentricity of the ellipsoidal structure only. q^* references to the interference maximum where interparticle interactions become more significant and N_{agg} is the aggregation number for the micelle. A polydispersity of 0.1 was applied to all polar and equatorial radii to account for a polydisperse micellar population.

***cis*-AzoTAB**	**Conc. (mM)**	**Form factor $P(q)$**	***R*** **(Å)**	***L*** **(Å)**	***H*** **(Å)**	***ε***	***q**** **(Å^{-1})**	N_{agg}
C_4AzoOC_2TAB[a]	10	Ellipsoid	21	32				
C_4AzoOC_4TAB	5	Concentration too close to the CMC to yield useful scattering profile						
	20	Sphere[b]	26 ± 1	-	-	-	0.035	42 ± 8
C_4AzoOC_6TAB	5	Sphere	24 ± 1	-	-	-	-	26 ± 5
	20	Sphere[b]	26 ± 1	-	-	-	0.037	67 ± 10
C_8AzoOC_2TAB	5	Sphere	22 ± 1	-	-	-	-	47 ± 5
	20	Sphere[b]	25 ± 1	-	-	-	0.035	72 ± 10
C_8AzoOC_6TAB	5	Sphere	28 ± 1	-	-	-	-	64 ± 8
	20	Oblate Ellipsoid[b]	23 ± 1	36 ± 1	-	0.77	0.035	140 ± 13
C_6AzoOC_4TAB	20	Elliptical Cylinder	22 ± 1	46 ± 1	260 ± 9	0.89	-	572 ± 25

[a] From Akamatsu *et al.*[37] [b] Hayter-Penfold structure factor for electrostatic interactions included in this fit as described in the text.

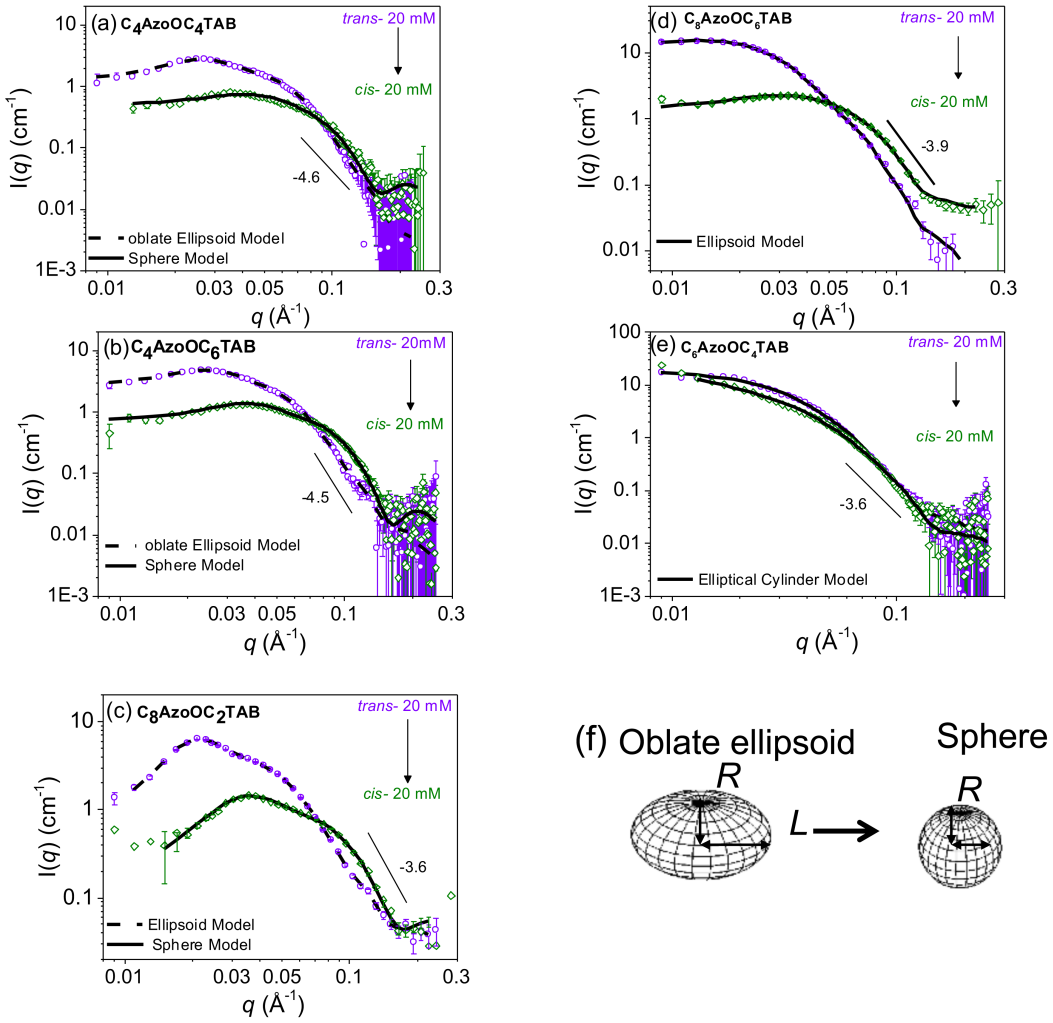

Figure 5. Effect of photoisomerization on the SANS profiles of AzoTABs in D_2O (20 mM, 20 °C). Scattering data presented for the *trans*- (purple circles) and *cis*-isomers (green diamonds) of (a) **C_4AzoOC$_4$TAB**, (b) **C_4AzoOC$_6$TAB**, (c) **C_8AzoOC$_2$TAB**, (d) **C_8AzoOC$_6$TAB** and (e) **C_6AzoOC$_4$TAB.** The solid and dashed black lines correspond to fits to the data as described in the text. (f) A model of the ellipse to sphere transition of AzoTAB micelles upon photoisomerization, where *R* is the polar radius and *L* is the equatorial radius.

Visualization of the Micelle Structure

Cryo-SEM measurements were performed on the images of the *trans*- and *cis*-isomers of **C_8AzoOC$_2$TAB** (20 mM). This AzoTAB was selected based on the large difference in the SANS scattering profiles observed upon photoisomerization. Figure 6 shows the cryo-SEM images of the *trans*- and *cis*-isomers of **C_8AzoOC$_2$TAB**. Image analysis revealed the presence of a primary population of aggregates with diameters of 7.5 ±1.0 nm and 4 ±0.5 nm for the *trans*- and *cis*-isomers, respectively (see Figure S26, SI). In addition, several very

large aggregates are observed, ~200 nm in diameter, which are believed to be artefacts of the sample preparation process (e.g. particle agglomeration and/or crystallisation of solid surfactant). Upon increasing magnification, the larger *trans*-aggregates appear to be populated with smaller aggregates on the surface (Figure 6b), while *cis*-form micelles are much smoother (Figure 6d). Increased magnification did not allow the smaller aggregates to be examined in detail, however they seem to match the sizes and shapes determined from the analysis of the SANS data. Finally, the *trans*-aggregates are isolated, while *cis*-aggregates are more closely packed, and in some cases lead to the formation of fused micelles (Figure 6c, green circle in Figure 6d). These observations agree with the SANS data, which show a shorter distance between aggregates upon photoisomerization. However, it cannot be excluded that these differences arise due to the stark contrast in the local environment of the micelles in the two techniques (liquid for SANS, cryogenic freezing and freeze-fracture for SEM).

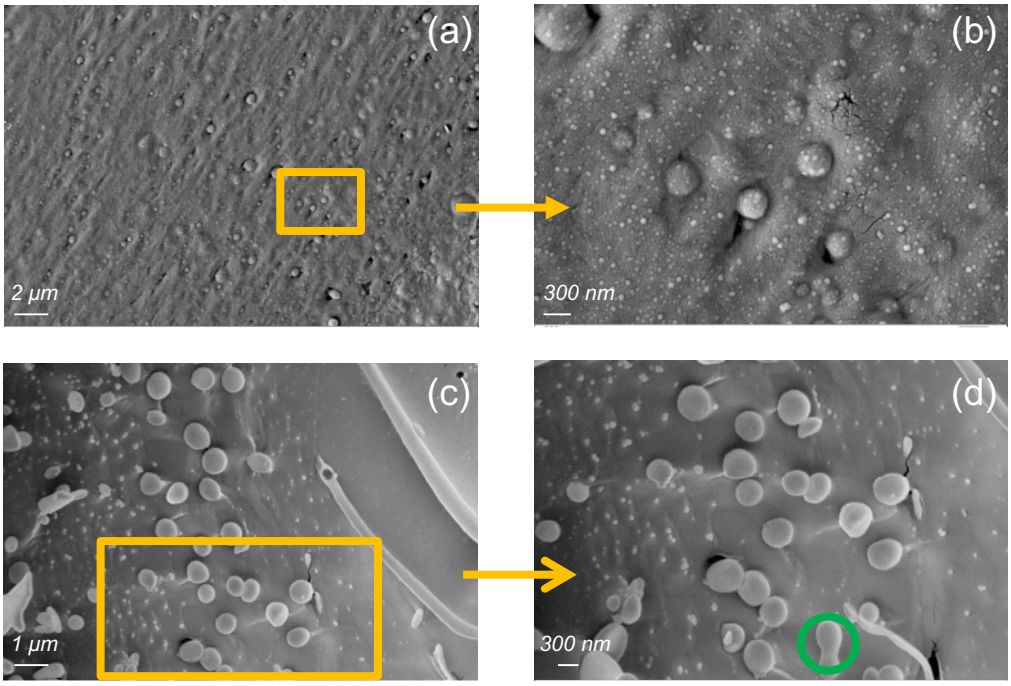

Figure 6. Examination of the aggregate structure of AzoTABs above the CMC (20 mM). Cryo-SEM images of (a), (b) *trans*-**C_8AzoOC_2TAB** and (c), (d) *cis*-**C_8AzoOC_2TAB**. Images (b) and (d) are magnified from the orange

boxes in images (a), (c) and (e), respectively. The green circle in (d) highlights the fusing of two aggregates. Scale bars have been added manually to the images for clarity and the image footers have been removed.

DISCUSSION

The surface activity and self-assembly characteristics of AzoTABs are controlled by subtle differences in the molecular structure. For *trans*-isomers, the total length of the hydrophobic segment, which comprises the alkyl tail, the Azo core and the spacer, determines the CMC and size of the micelles formed. For the *cis*-form, the composition of the hydrophobic segment is less clear cut. Photoisomerization to the *cis*-isomer leads to a decrease in the volume of the azobenzene core, which is accompanied by a significant increase in the dipole moment from 0 to 3 D.[19] This results in a significant hydrophilic component within the assumed hydrophobic tail. If the spacer length is reasonably short, photoisomerization will bring the *cis*-azobenzene core into closer proximity with the polar trimethylammonium bromide head group. In this conformation, it may be more intuitive to consider the polar Azo core and the short spacer as part of the hydrophilic head group, rather than the hydrophobic segment. If this is the case, it may be interesting to consider the maximum spacer length to which this behaviour occurs.

Like conventional surfactants, the value of the CMC is primarily determined by the length of the alkyl chain, with long chains leading to a lower CMC. However, the effect of the molecular structure on the ΔCMC for the *cis*- and *trans*-isomers is less obvious. There is an apparent sweet spot in the length of the assumed hydrophobic segment for $R_1 + R_2 = 6$, which leads to the maximum difference in the CMCs between the two isomers. Previous SANS studies have shown that like most of the AzoTABs studied here, C_4AzoOC_2TAB also forms ellipsoidal (*trans*) or *pseudo*-spherical (*cis*) in D_2O (up to 50 mM).[37] The large difference in the ΔCMC is therefore unlikely to be due to the shape of the aggregate formed. For a given hydrophobic segment length ($R_1 + R_2 = 6$ or 10), the largest ΔCMC is always obtained for the

homologue with the longest spacer. To achieve a large ΔCMC, either the absolute value of the CMC_{trans} must decrease, or the CMC_{cis} must increase, or a combination of the two must occur. For a given homologous series, increasing the length of the spacer results in a corresponding decrease in the alkyl tail, which leads to an increase in the CMC. The CMC_{trans} therefore increases with the spacer length. The large ΔCMC must therefore arise from an increase in the CMC_{cis}. One possible explanation for this is that upon photoisomerization, the Azo core and spacer now form part of the effective hydrophilic segment of the molecule, and as such the increasing spacer length leads to a larger hydrophilic volume and a higher CMC. The interesting question is if there is a limit on the spacer length at which this transition to a large effective hydrophilic segment occurs and whether the same behaviour would be observed for spacers with an odd number of carbon atoms.

The shapes of the micelles obtained for the fitting of the SANS data to standard geometrical models are in good agreement with the shapes predicted based on the molecular structure using the theoretical packing parameter. With the exception of **C_6AzoOC$_4$TAB**, all AzoTABs studied here form ellipsoidal micelles in the *trans*-form and spherical micelles in the *cis*-form. For the *trans*-isomers, micellar growth occurs predominantly in the equatorial axis (L) and there is an apparent maximum micelle size for a given hydrophobic segment length (C_{10}: $L \approx 50$ Å), above which the formation of new aggregates is favoured over further growth. At a given concentration, the corresponding spherical *cis*-aggregates are wetter and have a lower N_{agg}. This is both consistent with a decrease in the molecular packing density within the aggregates due to the "kink" in the Azo core upon photoisomerization and also increased solvation of the effective hydrophilic segment, which based on the arguments above, is now larger in size.

In contrast to the other AzoTABs studied, **C_6AzoOC$_4$TAB** favours the formation of elliptical cylinders in D_2O in both the *trans*- and *cis*-forms, which is in contradiction to the

theoretical packing parameters for this molecule that predict ellipsoidal/spherical aggregates. However, for the *cis*-isomer in particular, severe estimates are made for the volume of the azobenzene core. Moreover, the head group area is limited to the cationic terminal group in these calculations, which may not be an accurate reflection of the true effective hydrophilic segment. Nevertheless, there is an apparent preference for **C_6AzoOC_4TAB** to form cylindrical micelles with a lower curvature and photoisomerization has a limited effect on the shape and size of the aggregates formed. It is as yet unclear which exact feature of the molecular structure drives this preference.

Finally, as noted earlier, photoisomerization does not lead to the formation of a 100% *cis*-population, and approximately 5% of the photostationary state is composed of *trans*-isomers. It is interesting to consider if discrete all-*trans* and all-*cis* aggregates form under these conditions. Cryo-SEM analysis of *cis*-**C_8AzoOC_2TAB** revealed that spherical aggregates comprise the primary aggregate population in this sample, however isolated ellipsoidal aggregates more characteristic of the *trans*-isomer were also observed. However, further work is required to further understand if this behaviour is true of the entire sample and also of all AzoTABs.

CONCLUSIONS

In summary, we have investigated the structure-function-self-assembly characteristics of AzoTAB photosurfactants, with a specific focus on the length and composition of the hydrophobic segment. Our studies, and comparison with the properties of known AzoTABs from the literature have revealed that modest changes in the molecular structure can lead to large variations in the CMC, particularly between the two isomeric forms, and also unexpected aggregate structures. Although these effects are not trivial to predict, subtle trends related to the absolute length of the alkyl tail and the spacer group have been identified.

Furthermore, it is apparent that photoisomerization leads to a dramatic increase in the hydrophilicity of the molecule, leading to higher CMCs and the formation of smaller and wetter aggregates. Our studies suggest that following photoisomerization, the hydrophobic segment is confined primarily to the alkyl tail, and that the azobenzene core and the spacer form part of the effective hydrophilic segment of the molecule. Further work is now required to investigate if this behavior is restricted to short spacer length, or whether this can be extended to much longer spacer lengths, which should lead to a dramatic shift in the hydrophobic-hydrophilic balance in the *trans* and *cis* isomers.

Our findings show that careful design of AzoTAB photosurfactants is needed to tune both the CMC and the nanoscale structure of the resultant micelles. This is of particular importance when selecting the correct surfactant structure for a specific application. For example, variation of the position of the azobenzene core within the hydrophobic segment enables the ΔCMC to be subtly optimised and clear alkyl chain/spacer combinations to maximize this property have been identified. The ΔCMC concept has been used recently for the recovery of carbon nanotubes[32] or solubilization of ethylbenzene[37] in aqueous media, using short AzoTABs (*e.g.* C_4AzoOC_2TAB and C_4AzoOC_4TAB, respectively) which leads to a large ΔCMC, but also requires a large amount of material. Conversely, an extended AzoTAB leads to a small ΔCMC but reduces the amount of material required. A large ΔCMC is desirable for the application of AzoTABs in micellar catalysis, as it may facilitate the recovery of product by simple UV light illumination[57] and leads to more flexibility in the design of the reaction. This property can be associated with the size and shape of micelles for the design of optimised light-activated nanocarriers for product release.

ASSOCIATED CONTENT

Supporting Information

The Supporting Information is available free of charge on the ACS Publications website.

Materials; synthesis and structural characterization of AzoTABs; UV/Vis absorption spectroscopy of AzoTABs; determination of the CMC (ST and DLS data); small-angle neutron scattering; model dependant and independent analysis; procedure to validate SANS model fits; calculation of the packing parameter of AzoTABs.

AUTHOR INFORMATION

Corresponding Author
*E-mail: rce26@cam.ca.uk. Tel: +44 1223 334356.

Notes
The authors declare no competing financial interest.

ACKNOWLEDGMENTS

We thank Dr Clodagh Dooley for assistance with the cryo-SEM. CB thanks Trinity College Dublin for the award of a postgraduate studentship. Experiments at the ISIS Pulsed Neutron and Muon Source were supported by a beamtime allocation from the Science and Technology Facilities Council (Experiment: RB1610028, DOI: 10.5286/ISIS.E.79106883 and 10.5286/ISIS.E.82352186). This work benefited from the use of the SasView application, originally developed under NSF award DMR-0520547. SasView also contains code developed with funding from the European Union's Horizon 2020 research and innovation programme under the SINE2020 project, grant agreement No 654000.

REFERENCES

(1) Mao, Y.; Ding, Z.; Yuan, C.; Ai, S.; Isakov, M.; Wu, J.; Wang, T.; Dunn, M. L.; Qi, H. J. 3D Printed Reversible Shape Changing Components with Stimuli Responsive Materials. *Sci. Rep.* **2016**, *6*, 24761.
(2) Angelos, S.; Johansson, E.; Stoddart, J. F.; Zink, J. I. Mesostructured silica supports for functional materials and molecular machines. *Adv. Funct. Mater.* **2007**, *17*, 2261-2271.
(3) Islam, M. R.; Li, X.; Smyth, K.; Serpe, M. J. Polymer-Based Muscle Expansion and Contraction. *Angew. Chem. Int. Ed.* **2013**, *52*, 10330-10333.
(4) Angelos, S.; Choi, E.; Vögtle, F.; De Cola, L.; Zink, J. I. Photo-Driven Expulsion of Molecules from Mesostructured Silica Nanoparticles. *J. Phys. Chem. C* **2007**, *111*, 6589-6592.

(5) Nguyen, T. D.; Leung, K. C. F.; Liong, M.; Liu, Y.; Stoddart, J. F.; Zink, J. I. Versatile Supramolecular Nanovalves Reconfigured for Light Activation. *Adv. Funct. Mater.* **2007**, *17*, 2101-2110.
(6) Nguyen, T. D.; Leung, K. C. F.; Liong, M.; Pentecost, C. D.; Stoddart, J. F.; Zink, J. I. Construction of a pH-Driven Supramolecular Nanovalve. *Org. Lett.* **2006**, *8*, 3363-3366.
(7) Lu, Y.; Sun, W.; Gu, Z. Stimuli-responsive nanomaterials for therapeutic protein delivery. *J. Control. Release* **2014**, *194*, 1-19.
(8) Diguet, A.; Guillermic, R. M.; Magome, N.; Saint-Jalmes, A.; Chen, Y.; Yoshikawa, K.; Baigl, D. Photomanipulation of a droplet by the chromocapillary effect. *Angew. Chem.* **2009**, *121*, 9445-9448.
(9) Kumar, G. S.; Neckers, D. C. Photochemistry of azobenzene-containing polymers. *Chem. Rev.* **1989**, *89*, 1915-1925.
(10) Zhao, Y.; Ikeda, T. *Smart light-responsive materials: azobenzene-containing polymers and liquid crystals*; John Wiley & Sons: Hoboken, New Jersey, 2009.
(11) El Halabieh, R. H.; Mermut, O.; Barrett, C. J. Using light to control physical properties of polymers and surfaces with azobenzene chromophores. *Pure Appl. Chem.* **2004**, *76*, 1445-1465.
(12) Eastoe, J.; Vesperinas, A. Self-assembly of light-sensitive surfactants. *Soft Matter* **2005**, *1*, 338-347.
(13) Svetlana, S. Remote control of soft nano-objects by light using azobenzene containing surfactants. *J. Phys. D: Appl. Phys.* **2018**, *51*, 013002.
(14) Fomina, N.; Sankaranarayanan, J.; Almutairi, A. Photochemical mechanisms of light-triggered release from nanocarriers. *Adv. Drug Deliv. Rev.* **2012**, *64*, 1005-1020.
(15) Leonard, E.; Mangin, F.; Villette, C.; Billamboz, M.; Len, C. Azobenzenes and catalysis. *Catal. Sci. Technol.* **2016**, *6*, 379-398.
(16) Holmberg, K.; Jönsson, B.; Kronberg, B.; Lindman, B. *Surfactants and polymers in aqueous solution*; Wiley Online Library: New York, 2003.
(17) Moroi, Y. *Micelles: Theoretical and Applied Aspects*; Plenum: New York, 1992.
(18) Merino, E.; Ribagorda, M. Control over molecular motion using the cis–trans photoisomerization of the azo group. *Beilstein J. Org. Chem.* **2012**, *8*, 1071-1090.
(19) Hartley, G. S.; Le Fevre, R. J. W. 119. The dipole moments of cis- and trans-azobenzenes and of some related compounds. *Journal of the Chemical Society (Resumed)* **1939**, 531-535.
(20) Tabor, R. F.; Pottage, M. J.; Garvey, C. J.; Wilkinson, B. L. Light-induced structural evolution of photoswitchable carbohydrate-based surfactant micelles. *Chem. Commun.* **2015**, *51*, 5509-5512.
(21) Peng, S.; Guo, Q.; Hartley, P. G.; Hughes, T. C. Azobenzene moiety variation directing self-assembly and photoresponsive behavior of azo-surfactants. *J. Mater. Chem. C* **2014**, *2*, 8303-8312.
(22) Bandara, H. M. D.; Burdette, S. C. Photoisomerization in different classes of azobenzene. *Chem. Soc. Rev.* **2012**, *41*, 1809-1825.
(23) Tan, X.; Zhang, R.; Guo, C.; Cheng, X.; Gao, H.; Liu, F.; Bruckner, J. R.; Giesselmann, F.; Prehm, M.; Tschierske, C. Amphotropic azobenzene derivatives with oligooxyethylene and glycerol based polar groups. *J. Mater. Chem. C* **2015**, *3*, 11202-11211.
(24) Tabor, R. F.; Tan, D. D.; Han, S. S.; Young, S. A.; Seeger, Z. L. E.; Pottage, M. J.; Garvey, C. J.; Wilkinson, B. L. Reversible pH- and Photocontrollable Carbohydrate-Based Surfactants. *Chem. Eur. J.* **2014**, *20*, 13881-13884.
(25) Richter, M.; Zakrevskyy, Y.; Eisele, M.; Lomadze, N.; Santer, S.; Von Klitzing, R. Effect of pH, co-monomer content, and surfactant structure on the swelling behavior of microgel-azobenzene-containing surfactant complex. *Polymer* **2014**, *55*, 6513-6518.
(26) Lee, C. T.; Smith, K. A.; Hatton, T. A. Photoreversible viscosity changes and gelation in mixtures of hydrophobically modified polyelectrolytes and photosensitive surfactants. *Macromolecules* **2004**, *37*, 5397-5405.
(27) Schimka, S.; Lomadze, N.; Rabe, M.; Kopyshev, A.; Lehmann, M.; von Klitzing, R.; Rumyantsev, A. M.; Kramarenko, E. Y.; Santer, S. Photosensitive microgels containing azobenzene surfactants of different charges. *Phys. Chem. Chem. Phys.* **2017**, *19*, 108-117.
(28) Le Ny, A. L. M.; Lee, C. T. Conformation and dynamics of DNA molecules during photoreversible condensation. *Biophys. Chem.* **2009**, *142*, 76-83.

(29) Zakrevskyy, Y.; Roxlau, J.; Brezesinski, G.; Lomadze, N.; Santer, S. Photosensitive surfactants: Micellization and interaction with DNA. *J. Chem. Phys.* **2014**, *140*, 044906.
(30) Diguet, A.; Mani, N. K.; Geoffroy, M.; Sollogoub, M.; Baigl, D. Photosensitive surfactants with various hydrophobic tail lengths for the photocontrol of genomic DNA conformation with improved efficiency. *Chem. Eur. J.* **2010**, *16*, 11890-11896.
(31) Chen, S.; Bao, L.; Ou, E.; Peng, C.; Wang, W.; Xu, W. A cationic azobenzene-surfactant-modified graphene hybrid: unique photoresponse and electrochemical behavior. *Nanoscale* **2015**, *7*, 19673-19686.
(32) McCoy, T. M.; Liu, A. C. Y.; Tabor, R. F. Light-controllable dispersion and recovery of graphenes and carbon nanotubes using a photo-switchable surfactant. *Nanoscale* **2016**, *8*, 6969-6974.
(33) Wei, J.; Liu, Y.; Chen, J.; Li, Y.; Yue, Q.; Pan, G.; Yu, Y.; Deng, Y.; Zhao, D. Azobenzene-Derived Surfactants as Phototriggered Recyclable Templates for the Synthesis of Ordered Mesoporous Silica Nanospheres. *Adv. Mater.* **2014**, *26*, 1782-1787.
(34) Guo, Y.; Gong, Y.; Gao, Y. a.; Xiao, J.; Wang, T.; Yu, L. Multi-stimuli Responsive Supramolecular Structures Based on Azobenzene Surfactant-Encapsulated Polyoxometalate. *Langmuir* **2016**, *32*, 9293-9300.
(35) Hayashita, T.; Kurosawa, T.; Miyata, T.; Tanaka, K.; Igawa, M. Effect of structural variation within cationic azo-surfactant upon photoresponsive function in aqueous solution. *Colloid. Polym. Sci.* **1994**, *272*, 1611-1619.
(36) Zakrevskyy, Y.; Titov, E.; Lomadze, N.; Santer, S. Phase diagrams of DNA–photosensitive surfactant complexes: Effect of ionic strength and surfactant structure. *J. Chem. Phys.* **2014**, *141*, 164904.
(37) Akamatsu, M.; FitzGerald, P. A.; Shiina, M.; Misono, T.; Tsuchiya, K.; Sakai, K.; Abe, M.; Warr, G. G.; Sakai, H. Micelle Structure in a Photoresponsive Surfactant with and without Solubilized Ethylbenzene from Small-Angle Neutron Scattering. *J. Phys. Chem. B* **2015**, *119*, 5904-5910.
(38) Lund, R.; Brun, G.; Chevallier, E.; Narayanan, T.; Tribet, C. Kinetics of Photocontrollable Micelles: Light-Induced Self-Assembly and Disassembly of Azobenzene-Based Surfactants Revealed by TR-SAXS. *Langmuir* **2016**, *32*, 2539-2548.
(39) Israelachvili, J. N.; Mitchell, D. J.; Ninham, B. W. Theory of self-assembly of hydrocarbon amphiphiles into micelles and bilayers. *J. Chem. Soc., Faraday Trans. 2* **1976**, *72*, 1525-1568.
(40) Chevallier, E.; Monteux, C.; Lequeux, F.; Tribet, C. Photofoams: Remote Control of Foam Destabilization by Exposure to Light Using an Azobenzene Surfactant. *Langmuir* **2012**, *28*, 2308-2312.
(41) Zakrevskyy, Y.; Kopyshev, A.; Lomadze, N.; Morozova, E.; Lysyakova, L.; Kasyanenko, N.; Santer, S. DNA compaction by azobenzene-containing surfactant. *Phys. Rev. E* **2011**, *84*, 021909.
(42) Heenan, R. K.; Penfold, J.; King, S. M. SANS at Pulsed Neutron Sources: Present and Future Prospects. *J. Appl. Crystallogr.* **1997**, *30*, 1140-1147.
(43) http://www.mantidproject.org.
(44) Wignall, G. D.; Bates, F. S. Absolute calibration of small-angle neutron scattering data. *J. Appl. Crystallogr.* **1987**, *20*, 28-40.
(45) Pedersen, J. S. Analysis of small-angle scattering data from colloids and polymer solutions: modeling and least-squares fitting. *Adv. Colloid Interface Sci.* **1997**, *70*, 171-210.
(46) Feigin, L. A.; Svergun, D. I. *Structure Analysis by Small-Angle X-Ray and Neutron Scattering*; Plenum Press: New York, 1987.
(47) http://www.sasview.org/about.html.
(48) Orihara, Y.; Matsumura, A.; Saito, Y.; Ogawa, N.; Saji, T.; Yamaguchi, A.; Sakai, H.; Abe, M. Reversible Release Control of an Oily Substance Using Photoresponsive Micelles. *Langmuir* **2001**, *17*, 6072-6076.
(49) Yang, L.; Takisawa, N.; Hayashita, T.; Shirahama, K. Colloid Chemical Characterization of the Photosurfactant 4-Ethylazobenzene 4'-(Oxyethyl)trimethylammonium Bromide. *J. Phys. Chem.* **1995**, *99*, 8799-8803.
(50) Gelbart, W. M.; Ben-Shaul, A.; Roux, D. *Micelles, membranes, microemulsions, and monolayers*; Springer Science & Business Media: New York, 1994.

(51) Tanford, C. Micelle shape and size. *J. Phys. Chem.* **1972**, *76*, 3020-3024.
(52) Warr, G. G.; Sen, R.; Evans, D. F.; Trend, J. E. Microemulsion formation and phase behavior of dialkydimethylammonium bromide surfactants. *J. Phys. Chem.* **1988**, *92*, 774-783.
(53) Dutt, S.; Siril, P. F.; Remita, S. Swollen liquid crystals (SLCs): a versatile template for the synthesis of nano structured materials. *RSC Adv.* **2017**, *7*, 5733-5750.
(54) Butt, H.-J.; Graf, K.; Kappl, M. *Physics and Chemistry of Interfaces*; Wiley-VCH New York, 2004.
(55) Manojlović, J. Ž. The Krafft temperature of surfactant solutions. *Therm. Sci.* **2012**, *16*, S631–S640.
(56) Jain, N.; Trabelsi, S.; Guillot, S.; McLoughlin, D.; Langevin, D.; Letellier, P.; Turmine, M. Critical Aggregation Concentration in Mixed Solutions of Anionic Polyelectrolytes and Cationic Surfactants. *Langmuir* **2004**, *20*, 8496-8503.
(57) Billamboz, M.; Mangin, F.; Drillaud, N.; Chevrin-Villette, C.; Banaszak-Léonard, E.; Len, C. Micellar Catalysis Using a Photochromic Surfactant: Application to the Pd-Catalyzed Tsuji–Trost Reaction in Water. *J. Org. Chem.* **2014**, *79*, 493-500.
(58) Kano, K.; Tanaka, Y.; Ogawa, T.; Shimomura, M.; Okahata, Y.; Kunitake, T. Photoresponsive membranes. Regulation of membrane properties by photoreversible cis–trans isomerization of azobenzenes. *Chem. Lett.* **1980**, *9*, 421-424.
(59) Zemb, T.; Charpin, P. Micellar structure from comparison of X-ray and neutron small-angle scattering. *J .Phys. Fr.* **1985**, *46*, 249-256.
(60) Sivia, D. S. *Elementary Scattering Theory: For X-ray and Neutron Users*; Oxford University Press: New York, 2011.
(61) Bergstrom, L. M.; Grillo, I. Correlation between the geometrical shape and growth behaviour of surfactant micelles investigated with small-angle neutron scattering. *Soft Matter* **2014**, *10*, 9362-9372.
(62) Jackson, A. J. Introduction to Small-Angle Neutron Scattering and Neutron Reflectometry. *NIST Center for Neutron Research, Gaithersburg* **2008**, *12*.
(63) Dreiss, C. A. Wormlike micelles: where do we stand? Recent developments, linear rheology and scattering techniques. *Soft Matter* **2007**, *3*, 956-970.
(64) Hayter, J. B.; Penfold, J. An analytic structure factor for macroion solutions. *Mol. Phys.* **1981**, *42*, 109-118.
(65) Oliver, R. C.; Lipfert, J.; Fox, D. A.; Lo, R. H.; Doniach, S.; Columbus, L. Dependence of micelle size and shape on detergent alkyl chain length and head group. *PLoS One* **2013**, *8*, No. e62488.
(66) le Maire, M.; Champeil, P.; Møller, J. V. Interaction of membrane proteins and lipids with solubilizing detergents. *Biochim. Biophys. Acta.* **2000**, *1508*, 86-111.

TABLE OF CONTENTS